JOURNAL OF SPACECRAFT AND ROCKETS
Vol. 38, No. 4, July–August 2001

Two-Dimensional Implicit Thermal Response and Ablation Program for Charring Materials

Y.-K. Chen* and F. S. Milos†
NASA Ames Research Center, Moffett Field, California 94035-1000

The TITAN program for predicting charring material ablation and shape change of thermal protection materials is presented. The governing equations include energy conservation and a three-component decomposition model. The surface energy balance condition is solved with a moving grid to calculate the shape change due to surface recession. The governing equations are discretized with a finite volume approximation with a general body-fitted coordinate system. A time-accurate solution is achieved by an implicit time-marching technique with Gauss–Seidel line relaxation with alternating sweeps. Benchmark solutions are calculated and compared with available solutions to check code consistency and accuracy. For fully coupled solid–fluid simulation, this technique has been directly integrated with both a high-fidelity Navier–Stokes solver and an aerothermal flowfield engineering correlation code. Representative computations, including a slender hypersonic reentry vehicle and a flat-faced cylinder model in an arcjet test, are presented and discussed in detail.

Nomenclature

A = area, m^2
B_a = preexponential constant in Eq. (6), s^{-1}
B' = dimensionless mass blowing rate, $\dot{m}/\rho_e u_e C_M$
C_H = Stanton number for heat transfer
C_M = Stanton number for mass transfer
c_p = specific heat, J/kg · K
E_a = activation energy in Eq. (6), J/kmol
F = radiation view factor in Eq. (8)
H_r = recovery enthalpy, J/kg
h = enthalpy, J/kg
$\bar{h}$ = partial heat of charring, defined in Eq. (4), J/kg
k = thermal conductivity, W/m · K
$\dot{m}$ = mass flux, kg/m^2· s
P = pressure, N/m^2
q_C = conductive heat flux, W/m^2
q_R = radiative heat flux, W/m^2
R = universal gas constant, J/kmol · K
R_c = corner radius, m
R_n = nose radius, m
s = surface recession, m
$\dot{s}$ = surface recession rate, m/s
T = temperature, K
t = time, s
u = velocity, m/s
v = local grid velocity, m/s
Z^* = coefficient in Eq. (8), defined in Ref. 11
α = surface absorptance
Γ = volume fraction of resin
ε = surface emissivity
λ = blowing reduction parameter
ξ, η = general body-fitted coordinate system
ρ = total density, kg/m^3
σ = Stefan–Boltzmann constant, W/m^2 · K^4
τ = mass fraction of virgin material, defined in Eq. (3)
ϕ = vector of independent variables, defined in Eq. (12)
Ψ = decomposition reaction order in Eq. (6)

Subscripts

c = char
e = boundary-layer edge
g = pyrolysis gas
i = density component (A, B, and C)
j = surface species
m, n = index of computation cell
v = virgin
w = wall

Superscripts

ℓ = index of time level

Introduction

SPACECRAFT heatshields typically use thermal protection system (TPS) materials that pyrolyze and ablate at high temperature for mass-efficient rejection of the aerothermal heat load. Pyrolysis is an internal decomposition of the solid that releases gaseous species, whereas ablation is a combination of processes that consume heatshield surface material. For the design and sizing of ablating spacecraft TPS materials, it is imperative to have a reliable numerical procedure that can compute surface recession rate, in-depth pyrolysis, and internal temperature histories under general heating conditions.

CMA[1] was developed by the Aerotherm Corporation in the 1960s. This technique solved the internal energy balance and decomposition equations, coupled with the ablating surface energy balance condition, to simulate the response of ablative heatshields in hypersonic flows. Recently, FIAT was developed at NASA Ames Research Center.[2] FIAT is numerically more stable and solves a wider range of problems compared with CMA, and it has been used for TPS sizing calculations for various NASA space missions, for example, Mars Pathfinder and Stardust.[2] However, the governing equations solved in both CMA and FIAT codes are one-dimensional. Thus, these two codes are not reliable for conditions in which the one-dimensional assumption is not true, such as a nosetip of a slender hypersonic reentry vehicle or an arcjet test model with small nose radius.

ASCC,[3] also developed by the Aerotherm Corporation, is an engineering code for fully coupled solid–fluid simulation with two-dimensional (axisymmetric or planar) geometry. In ASCC, the effect of pyrolysis gas from internal decomposition is not implemented, and the thermal diffusion equation is solved using a finite difference scheme with overlaid grids that is not always accurate.[4] A two-dimensional ablation code developed at Sandia National

Presented as Paper 2000-0206 at the AIAA 38th Aerospace Sciences Meeting, Reno, NV, 10–13 January 2000; received 11 May 2000; revision received 13 February 2001; accepted for publication 14 February 2001.

*Aerospace Engineer, Thermal Protection Materials and Systems Branch. MS 234-1; ykchen@mail.arc.nasa.gov.

†Ceramic Engineer, Thermal Protection Materials and Systems Branch. MS 234-1; fmilos@mail.arc.nasa.gov. Senior Member AIAA.

Laboratories uses the finite control volume method with unstructured grids.[5] In this code, mesh motion owing to ablation is implemented by assuming the mesh behaves as a linear elastic solid with surface-node displacement equal to the surface recession. The effect of pyrolysis gas was not considered, however, and the solid–fluid interaction was not discussed. More recent work considered different iterative approaches for coupling the fluid and solid solutions.[6]

The subject of this work is the development of the TITAN program to perform high-fidelity thermal response and shape change simulations for charring materials. The governing equations, which include energy conservation and a three-component decomposition model with a moving grid, are discretized using a finite volume approximation with general body-fitted coordinates. A time-accurate solution is achieved by an implicit time-marching technique using Gauss–Seidel line relaxation with alternating sweeps.[7] The computational grid consists of an interior zone and an exterior zone. The interior zone remains fixed in the course of computation, whereas the exterior zone is compressed to account for surface ablation. In most cases, a coupled fluid–solid simulation is required for accurate prediction of shape change, because the aerothermal heating is very sensitive to the geometry of solid surface. The Navier–Stokes solver[8] GIANTS and the aerothermal flowfield engineering correlation code[3] MEIT are directly integrated with TITAN using a loosely coupled method for simulation of the solid–fluid interaction. Representative computations, including a slender nosetip and a flat-faced cylinder, will be presented and discussed in detail.

Governing Equations

The internal energy balance is a transient thermal conduction equation with additional pyrolysis terms[9]:

$$\rho c_p \frac{\partial T}{\partial t} = \nabla \cdot (k \nabla T) - (h_g - \bar{h}) \nabla \cdot \dot{m}_g + \dot{m}_g \cdot \nabla h_g + \rho c_p v \cdot \nabla T \tag{1}$$

The individual terms in Eq. (1) may be interpreted as follows: rate of storage of sensible energy, net rate of thermal conductive heat flux, pyrolysis energy consumption rate, net rate of energy convected by pyrolysis, and convection rate of sensible energy due to coordinate system movement. The local specific heat is formulated from functions of temperature input for both virgin material and charred. In partially pyrolyzed zones ($\rho_c < \rho < \rho_v$), the specific heat is obtained from a special mixing rule:

$$c_p = \tau c_{pv} + (1 - \tau) c_{pc} \tag{2}$$

where the weight variable τ is the mass fraction of virgin material in a mixture of virgin material and char that yields the correct local density

$$\tau = \frac{\rho_v (\rho - \rho_c)}{\rho (\rho_v - \rho_c)} \tag{3}$$

The thermal conductivity k is weighted in the same manner. The pyrolysis gas enthalpy h_g is input as a function of temperature and pressure. The quantity $\bar{h}$ is defined as

$$\bar{h} = \frac{\rho_v h_v - \rho_c h_c}{\rho_v - \rho_c} \tag{4}$$

The thermal and mechanical properties of many ablators for spacecraft heatshield applications are available in the TPSX program[10] accessible through the Internet.

A three-component decomposition model[9] is used. The resin filler is presumed to consist of two components that decompose separately, whereas the reinforcing material is the third component that can decompose. The instantaneous density of the composite is given by

$$\rho = \Gamma(\rho_A + \rho_B) + (1 - \Gamma)\rho_C \tag{5}$$

where A and B represent components of the resin and C represents the reinforcing material. The parameter Γ is the volume fraction of resin and is an input quantity. Each of the three components can decompose following the relation

$$\frac{\partial \rho_i}{\partial t} = -B_{ai} \exp\left(-\frac{Eai}{RT}\right) \rho_{oi} \left(\frac{\rho_i - \rho_{ri}}{\rho_{oi}}\right)^{\Psi_i} + v \cdot \nabla \rho_i \tag{6}$$

where ρ_{ri} is the residual or terminal density of component i, and ρ_{oi} is the original density of component i. The motion of pyrolysis gas is assumed to be one-dimensional (along the η direction), and, thus, the mass flow rate of pyrolysis gas at the surface is calculated using the following approximation:

$$\dot{m}_g = \frac{-1}{A} \int_{\eta_0}^{\eta_w} \left(\frac{\partial \rho}{\partial t}\right) A \, \mathrm{d}\eta \tag{7}$$

Boundary Conditions

Conditions at the ablating surface are determined by convective and radiative heating and by surface thermochemical interactions with boundary-layer gases. The surface energy balance equation employed is of the convective transfer coefficient type and takes the following form[9]:

$$\rho_e u_e C_H (H_r - h_{ew}) + \rho_e u_e C_M \left[\sum \left(Z^*_{je} - Z^*_{jw}\right) h_j^{Tw} - B' h_w \right] + \dot{m}_c h_c + \dot{m}_g h_g + \alpha_w q_{Rw} - F \sigma \varepsilon_w T_w^4 - q_{Cw} = 0 \tag{8}$$

The first term in Eq. (8) represents the sensible convective heat flux. The sum of the second, third, and fourth terms in Eq. (8) is defined as the total chemical energy at the surface. The Z^* terms represent transport of chemical energy associated with chemical reactions at the wall and in the boundary layer.[11] The Z^* driving forces for diffusive mass transfer include the effects of unequal diffusion coefficients. The fifth and sixth terms are the radiative heat fluxes absorbed and reradiated by the wall, respectively, and the last term, q_{Cw}, represents the rate of conduction into the material. Here B' is the normalized mass blowing rate. Tables of B' for charring materials can be generated using the ACE[11] or MAT techniques.[12]

A blowing correction allows for the reduction in transfer coefficients due to the transpiration or blowing effect of gases from pyrolysis and surface ablation being injected into the boundary layer. The blowing rate correction equation for convective heat transfer is

$$C_H = C_{H1} \left[\frac{\ell n(1 + 2\lambda B')}{2\lambda B'} \right] \tag{9}$$

where λ is blowing reduction parameter, C_H is heat transfer coefficient for the ablating surface, and C_{H1} is the heat transfer coefficient for the nonablating surface. With $\lambda = 0.5$, Eq. (9) reduces to the classical laminar-flow blowing correction.[13] A variable λ is used for cases with transitional or turbulent flow.

Solution Procedure

Equation (1) is written in Cartesian coordinates. To make a transformation to a general body-fitted coordinate system (ξ and η), the chain rule of differentials is applied:

$$\frac{\partial}{\partial x} = \frac{\partial \xi}{\partial x}\frac{\partial}{\partial \xi} + \frac{\partial \eta}{\partial x}\frac{\partial}{\partial \eta}, \qquad \frac{\partial}{\partial y} = \frac{\partial \xi}{\partial y}\frac{\partial}{\partial \xi} + \frac{\partial \eta}{\partial y}\frac{\partial}{\partial \eta} \tag{10}$$

Equation (1) in a general body-fitted coordinate system may be written at cell (m, n) as

$$A_{m,n}\delta\phi^l_{m,n} + B_{m,n}\delta\phi^l_{m,n+1} + C_{m,n}\delta\phi^l_{m,n-1} = -D_{m,n}\delta\phi^l_{m+1,n} - E_{m,n}\delta\phi^l_{m-1,n} + \Delta\phi^l_{m,n} \tag{11}$$

where

$$\phi = [T, \rho_A, \rho_B, \rho_C], \qquad \Delta\phi^l_{m,n} = F_i \, \mathrm{d}t$$

$$A_{m,n} = \left(I - \left.\frac{\partial F_i}{\partial \phi_j}\right|_{m,n} \mathrm{d}t\right), \qquad B_{m,n} = -\left.\frac{\partial F_i}{\partial \phi_j}\right|_{m,n+1} \mathrm{d}t$$

$$C_{m,n} = -\left.\frac{\partial F_i}{\partial \phi_j}\right|_{m,n-1} \mathrm{d}t, \qquad D_{m,n} = -\left.\frac{\partial F_i}{\partial \phi_j}\right|_{m+1,n} \mathrm{d}t$$

$$E_{m,n} = -\left.\frac{\partial F_i}{\partial \phi_j}\right|_{m-1,n} \mathrm{d}t \tag{12}$$

In Eq. (12), I is the identity matrix and F_1 is the right-hand-side terms of Eq. (1) in the general coordinate system divided by ρc_p. F_2–F_4 are the right-hand-sideterms of Eq. (6) for components A–C, and subscripts i and $j = 1$–4.

Equation (11) may be solved by a block-tridiagonalmatrix inversion using Gauss–Seidel line relaxation with alternating sweeps in the backward and forward directions.[7] The backward sweep consists of the solution of

$$A_{m,n}\delta\phi^{(\ell)}_{m,n} + B_{m,n}\delta\phi^{(\ell)}_{m,n+1} + C_{m,n}\delta\phi^{(\ell)}_{m,n-1} = -D_{m,n}\delta\phi^{(\ell)}_{m+1,n} - E_{m,n}\delta\phi^{(\ell-1)}_{m-1,n} + \Delta\phi^{\ell}_{m,n} \tag{13a}$$

and the forward sweep solves

$$A_{m,n}\delta\phi^{(\ell)}_{m,n} + B_{m,n}\delta\phi^{(\ell)}_{m,n+1} + C_{m,n}\delta\phi^{(\ell)}_{m,n-1} = -D_{m,n}\delta\phi^{(\ell-1)}_{m+1,n} - E_{m,n}\delta\phi^{(\ell)}_{m-1,n} + \Delta\phi^{\ell}_{m,n} \tag{13b}$$

The time advancement of the solution proceeds as follows. The explicit change in the solution a time level ℓ is computed at all computational cell (m, n) locations and is stored. Then, first the backward sweep is performed from the last m line to the first. Equation (13a) is solved using a block-tridiagonal matrix inversion technique at each constant m line. The results for $\delta\phi^{\ell}_{m,n}$ are used as they become available. Next, the forward sweep is performed from the first m location to the last. Again, this involves the solution of a series of block-tridiagonal equations, Eq. (13b), during which the most recently available data for $\delta\phi^{\ell}_{m,n}$ are used. In this fashion, the solution may be advanced to time level $\ell + 1$ using $\phi^{\ell+1}_{m,n} = \phi^{\ell}_{m,n} + \delta\phi^{\ell}_{m,n}$.

If time accuracy is not of interest in the computation (e.g., nonablating, steady-state cases[4,14]) the time step Δt should be as large as possible, and the number of alternating sweeps in each time step should be one. A time-accurate solution can be achieved by increasing the number of alternating sweeps in each time step or by reducing the time step. The latter approach was found to be more computationally efficient; therefore, the default algorithm performs only one forward and one backward sweep per time step. The time-marching algorithm is adaptive, increasing or decreasing the time step as required to maintain good convergence while not exceeding user input values of the maximum time step and the maximum temperature change per time step at any node.

A typical computational grid for a flat-faced cylinder is shown in Fig. 1a, and that for a slender body is shown in Fig. 1b. The grid is divided into two zones: interior ($m = jp$–il and $n = 2$–jp-1) and exterior ($m = 2$–il and $n = jp$–jl). The computational cells in the interior zone remain fixed in the course of simulation, and those cells in the exterior zone are compressed in the η direction to account for surface recession. In the exterior zone, the backward sweep is performed from the backface ($m = il$) to the centerline ($m = 2$), and then the forward sweep is performed from the centerline to the backface. In the interior zone, the backward sweep starts from the backface ($m = il$) to the interface between interior and exterior zones ($m = jp$), and then the forward sweep is from the interface to the backface. The two grids presented in Fig. 1 are sufficient to provide good definition of the temperature history and shape change in response to the surface heating for all cases considered in this work. A grid resolution example for the most complex case is provided in the Appendix.

A fully coupled high-fidelity solid–fluid simulation is achieved by integrating TITAN with GIANTS using a loosely coupled technique. The numerical method adopted in the GIANTS code to solve the governing Navier–Stokes equations[7] is exactly the same as that used in the TITAN code. The aerothermal heating is very sensitive to the body geometry. Thus, when the maximum local surface recession exceeds a predefined criterion since the last surface heating update, a new computational fluid dynamics (CFD) grid is generated based on the current body geometry, and the CFD routine, GIANTS, is called to update the aerothermal heating environment. Each call to the CFD routine is a quasi-steady-statecalculation. In this work, the nonablating (cold wall) heating was calculated by GIANTS using a five-species air chemistry (N_2, O_2, NO, N, and O). As required on a case-by-case basis, an 11-species (or higher) model can be used. Unless noted otherwise, a blowing reduction parameter $\lambda = 0.5$ was used in TITAN to take into account the blockage due to mass blowing.

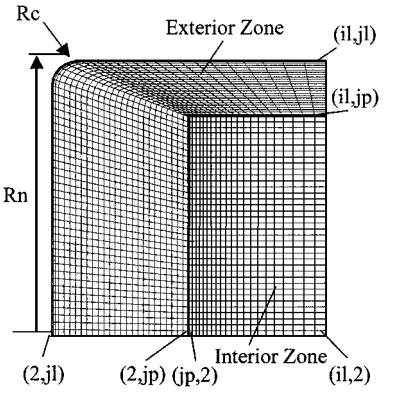

Fig. 1a Computational grid for flat-faced cylinder.

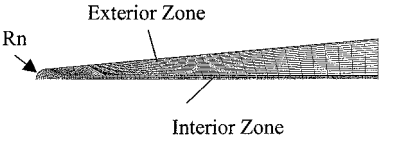

Fig. 1b Computational grid for slender body.

The CFD calculation is very computationally intensive compared with the thermal response computation. For a fully coupled simulation, most of the CPU time is consumed by the CFD portion of computation; therefore, the total CPU time and memory required is determined primarily by the efficiency of the CFD code.

Benchmark Solutions

Two groups of benchmark calculations are presented in this section. The first group considers multidimensional thermal conduction without ablation and shape change to check the accuracy of the thermal conduction solver that is the basic structure in the TITAN code. The results are compared with solutions obtained from the commercial finite element solver MARC[15] that has been validated elsewhere.[16] The second group of benchmark cases examines the pyrolysis gas and surface ablation models used in the TITAN code. Because there was no multidimensional charring material thermal response solution available for comparison, the conditions for an arcjet model, which is a flat-faced cylinder with 10.16-cm (4-in.) radius, are calculated using TITAN and the solution along the centerline is compared with the one-dimensional solution obtained with FIAT. (Solutions from FIAT have previously been checked against arcjet data and other available solutions.[2]) The TPS material properties used in the first group are those of ultrahigh-temperature ceramics[17] (UHTCs), and properties used in the second group are those of two advanced lightweight ceramic ablators, phenolic impregnated carbon ablator (PICA[18]) and silicone impregnated reusable ceramic ablator (SIRCA[19]), developed at NASA Ames Research Center.

Comparisons between TITAN and MARC solutions for an axisymmetric nosetip are presented in Figs. 2a and 2b. The nose radius R_n is 0.254 cm, the cone half angle is 5 deg, and the total length is 8.255 cm. A cold wall heat flux of 900 W/cm^2 was imposed on the spherical section of the nosetip, and the initial temperature was set to 300 K. The stagnation point temperature vs time and the steady-state centerline temperature vs distance are shown in Figs. 2a and 2b, respectively. A similar comparison for a planar geometry with

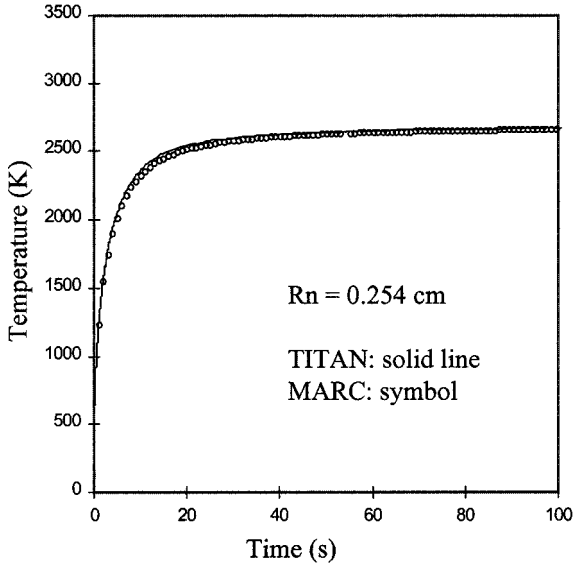

Fig. 2a Stagnation temperature history predicted for axisymmetric nosetip.

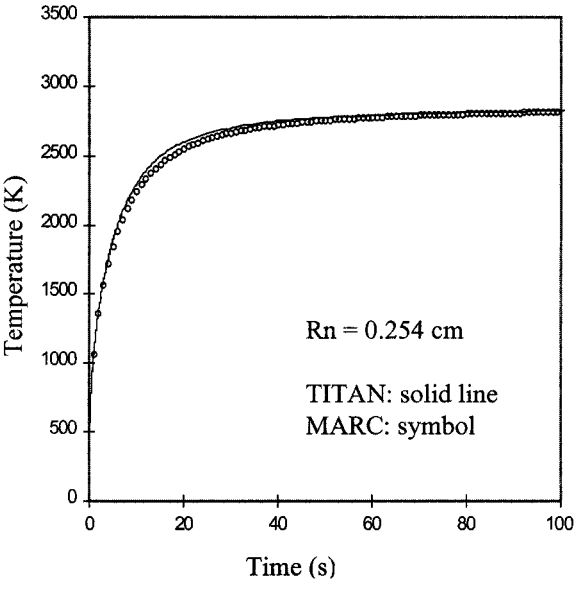

Fig. 3a Stagnation temperature history predicted for planar nosetip.

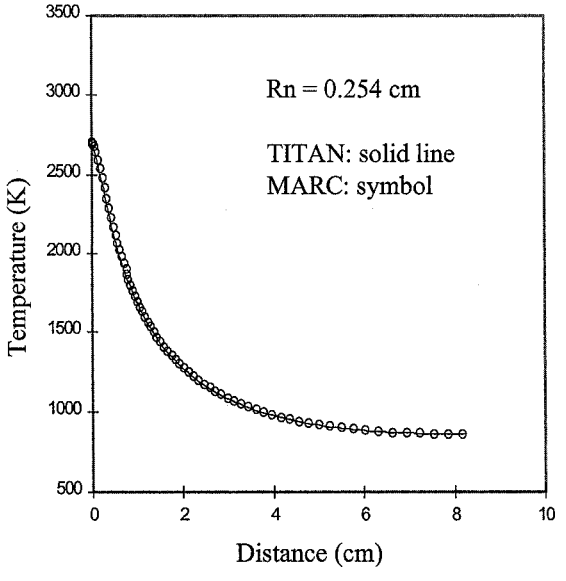

Fig. 2b Steady-state centerline temperature profile predicted for axisymmetric nosetip.

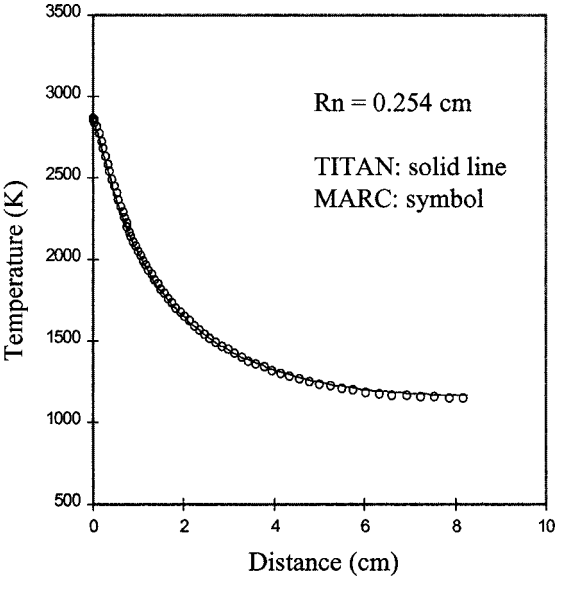

Fig. 3b Steady-state centerline temperature profile predicted for planar nosetip.

the same nose radius, total length, cold-wall heat flux, and material properties is presented in Figs. 3a and 3b. The results indicate that the thermal conduction solutions predicted from TITAN and MARC are in excellent agreement for both transient and steady-state conditions.

Predicted solutions for a flat-faced cylinder are shown in Figs. 4a and 4b. The cylinder radius is 0.635 cm, the corner radius is 0.158 cm, and the total length is 2.54 cm. A cold-wall heat flux of 900 W/cm^2 was imposed over the front flat face. The material properties are the same as those of the preceding cases. The stagnation point temperature history and the centerline steady-state temperature profile are presented in Figs. 4a and 4b, respectively. Again, there is good agreement between the thermal response predictions from the two codes.

To check the pyrolysis gas and surface ablation models in TITAN, test cases with a 10.16-cm-radius flat-faced cylinder were performed. The corner radius is one-tenth of cylinder radius, and the total length of cylinder is 5.08 cm. Because of the large cylinder radius, solutions near the centerline should approximately behave like a one-dimensional model.

The first case was calculated using SIRCA material properties and a cold-wall heat flux of 50 W/cm^2. The total length of the heat pulse was 60 s, and the surface pressure was 0.2 atm. The blowing reduction parameter was set to zero just to simplify the code-to-code comparison. Under these conditions, the surface recession is negligibly small, and, thus, the pyrolysis gas model can be examined alone. Figures 5a and 5b show the comparison between TITAN and FIAT results. The pyrolysis mass blowing rate at the stagnation point vs time is presented in Fig. 5a, and the temperature histories at the surface, and at depths of 2.54 and 5.08 cm, are shown in Fig. 5b. The results indicate that the TITAN solution with pyrolysis gas is consistent with the FIAT solution with pyrolysis.

The second test condition for the same geometry was performed using PICA material properties. In this case, to examine just the surface recession model, the internal decomposition rates were set to zero. The cold-wall heat flux was 445 W/cm^2, the surface pressure was 0.35 atm, and the length of heat pulse was 45 s. Centerline results from TITAN and FIAT are presented in Figs. 6a and 6b. Figure 6a displays the char mass blowing rate vs time, and Fig. 6b shows the temperature histories at the surface and at depths of 2.54 and

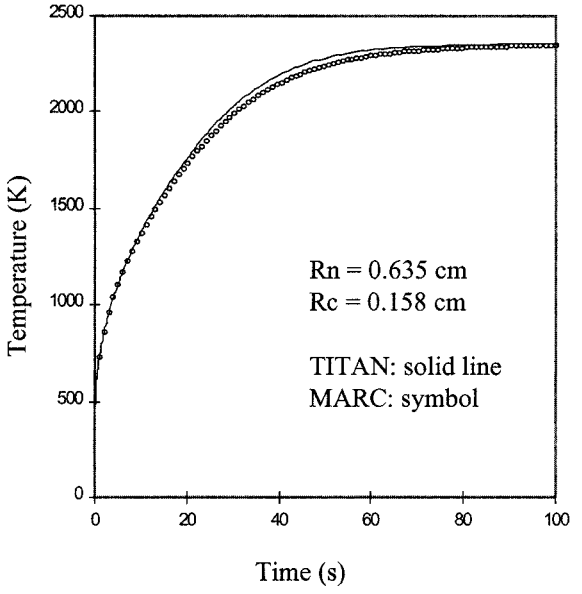

Fig. 4a Stagnation temperature history predicted for flat-faced cylinder.

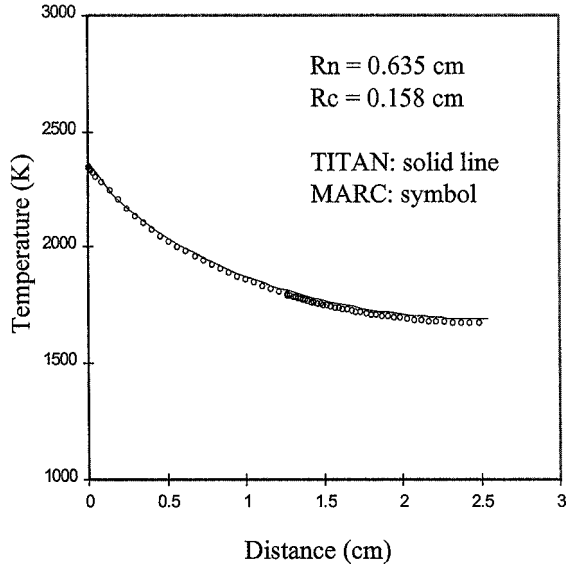

Fig. 4b Steady-state centerline temperature history predicted for flat-faced cylinder.

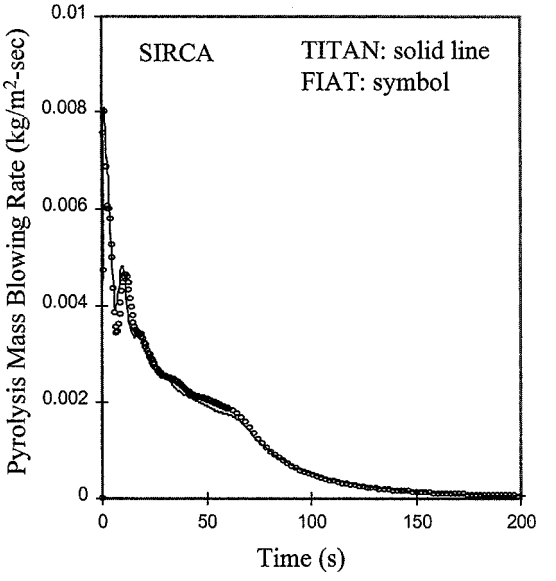

Fig. 5a Pyrolysis gas blowing rate predicted for SIRCA test case.

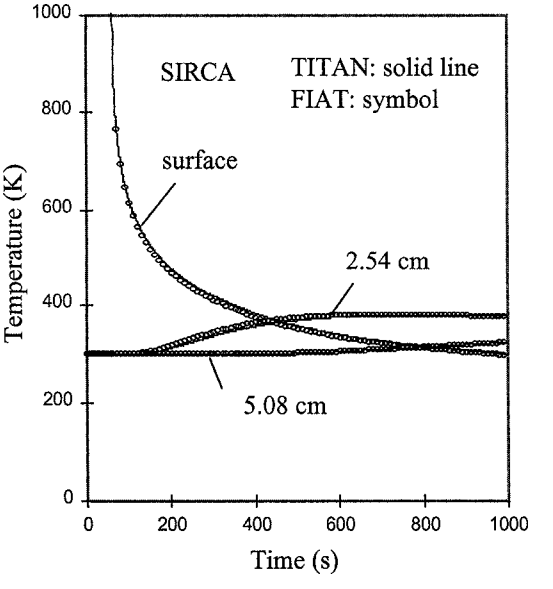

Fig. 5b Temperature histories predicted for SIRCA test case.

5.08 cm. The TITAN results agree well with FIAT predictions for this condition of surface recession without pyrolysis.

In the third case, the preceding computations were repeated using a complete PICA material model including both pyrolysis and ablation. The cold-wall heat flux was 270 W/cm^2, the surface pressure was 0.35 atm, and the length of heat pulse was 45 s. The blowing reduction parameter was again set to zero. The char and pyrolysis mass blowing rates vs time are shown in Fig. 7a, and temperature histories are shown in Fig. 7b. This final set of benchmark calculations confirms that TITAN solutions agree with FIAT with both pyrolysis gas and ablation effects included.

Fully Coupled Solid–Fluid Simulations

Two groups of fully coupled computations are presented in this section. The first group of solutions was obtained using the integrated TITAN/MEIT code, and the second group was computed using the integrated TITAN/GIANTS code. MEIT computations are relatively inexpensive compared with GIANTS. However, the correlations implemented in MEIT are only appropriate for a slender body with small cone angles. The accuracy of MEIT was examined in previous work[4] and will not be discussed in this paper.

A trajectory-based aerothermal analysis for a slender hypersonic reentry vehicle with a carbon-carbon nosetip was performed using TITAN/MEIT. Because there was no pyrolysis gas involved in this calculation, the TITAN prediction can be compared against an ASCC solution to check code consistency (with both codes using two-dimensional axisymmetric heat conduction). The initial nose radius was 2.18 cm, and the cone half angle was 9 deg. The trajectory used for this case is shown in Fig. 8a. The comparison of stagnation point temperature history between TITAN and ASCC is shown in Fig. 8b, and the shape change is presented in Fig. 8c. The predictions from TITAN and ASCC are generally in good agreement. The stagnation point temperature predicted by ASCC is slightly lower than that of TITAN. This result is consistent with previous work[4]: ASCC tends to underpredict the transient conduction into the material. Thus, the predicted recession from ASCC is slightly lower than that calculated by TITAN.

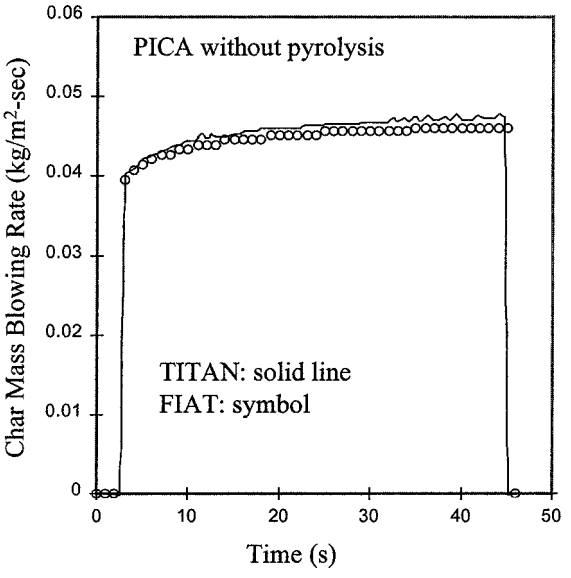

Fig. 6a Char-ablation blowing rate predicted for PICA test case without pyrolysis.

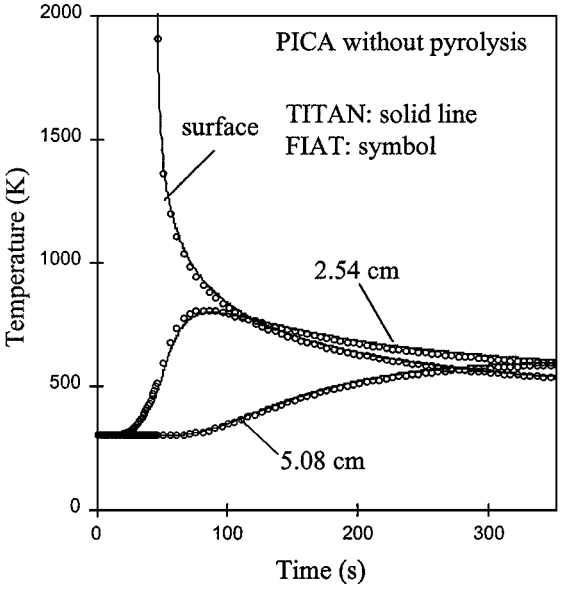

Fig. 6b Temperature histories predicted for PICA test case without pyrolysis.

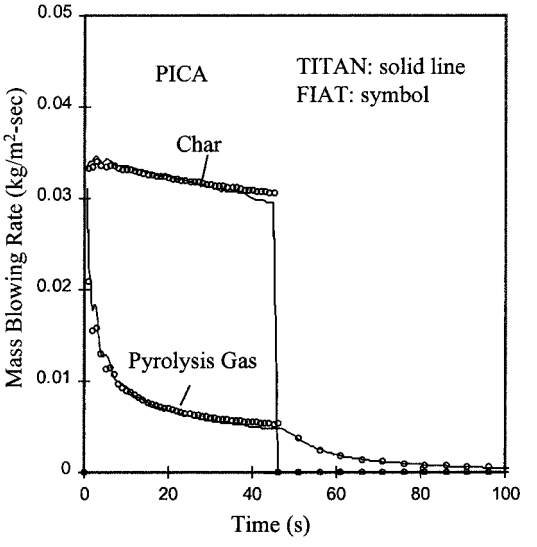

Fig. 7a Mass blowing rates predicted for final PICA test case.

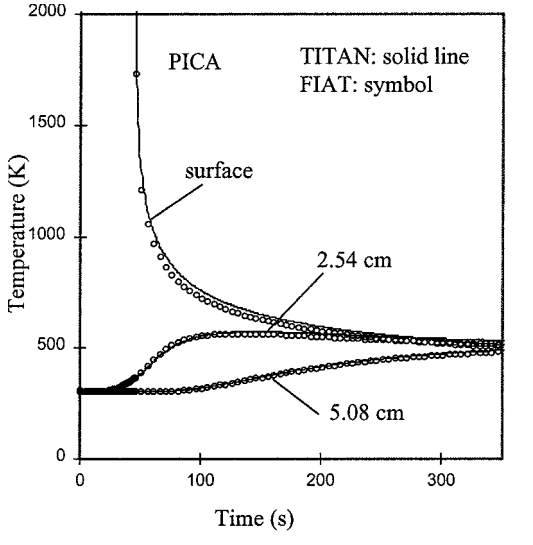

Fig. 7b Temperature histories predicted for final PICA test case.

The first test case calculated using TITAN/GIANTS was for a typical arcjet test model, which is a flat-faced cylinder with $R_n = 3.81$ cm, $R_c = 0.381$ cm, and a total length of 7.0 cm. The computational grid is shown in Fig. 9a. The TPS material is PICA, the model holder is Alumina Enhanced Thermal Barrier (AETB) tile, and the substructure is aluminum. First, the nonablating heat flux was calculated using GIANTS. This surface heating distribution is then imposed as part of initial surface boundary conditions for TITAN. The wall heat flux distribution at various times is shown in Fig. 9b. As expected, at $t = 0$ s the heating rate near the tangency point between the flat face and the corner is more than twice the stagnation point heating.

It is well known that the body shape and surface heating strongly affect each other. The surface contours of the fully coupled calculation at time = 0, 15, 25, and 35 s are presented in Fig. 9c. In this coupled calculation, a new CFD calculation was performed whenever the maximum surface recession exceeds 0.5% of the corner radius at the preceding CFD calculation. From numerical experiments with various criteria, it was found that this 0.5% criterion is sufficiently fine to resolve the solid shape change for this particular test case. The calculation shows that the aerothermal heating rounds the corner of test model, thereby reducing the corner heating while consequently increasing the heating in the stagnation region. The surface heating distribution gradually becomes more uniform (Fig. 9b) toward the end of heat pulse. This phenomenon was anticipated but was not studied previously because no high-fidelity, fully coupled solid–fluid simulation program was available. The initial stagnation-point heating was about 400 W/cm^2, and the final heating was slightly below 600 W/cm^2.

The second test case using TITAN/GIANTS is a slender body PICA nosetip with $R_n = 0.254$ cm, a cone half angle of 5 deg, and a total length of 8.255 cm. The criterion used for updating the aerothermal heating boundary condition was a change of 0.5% of the nose radius. From a CFD point of view, the computation of flow over a slender body is relatively easy compared with that over a flat-faced cylinder because there exists a large subsonic region over the entire front surface of the flat-faced cylinder. Thus, the CFD solution for a slender body converges at a much faster pace than that of the flat-faced cylinder. The cold-wall heat fluxes for the sharp nose at 0 and 25 s are shown in Fig. 10a. The initial stagnation point heating is slightly higher than 600 W/cm^2, and at the end of heat pulse (25 s) the stagnation-point heating is reduced to about 480 W/cm^2. The surface contours are shown in Fig. 10b. The flow gradually rounds the slender nosetip, and, consequently, the stagnation heating is reduced. This trend is opposite to that of flat-faced cylinder, where the stagnation-point heat flux increases with time (Fig. 9b). As the

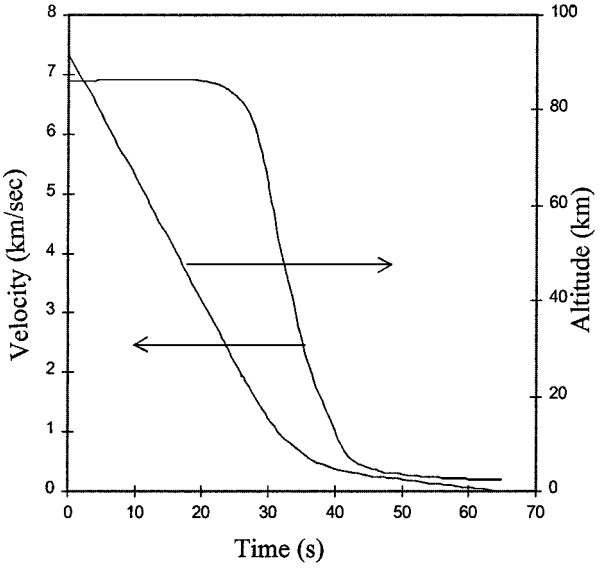

Fig. 8a Sample trajectory for slender hypersonic reentry vehicle.

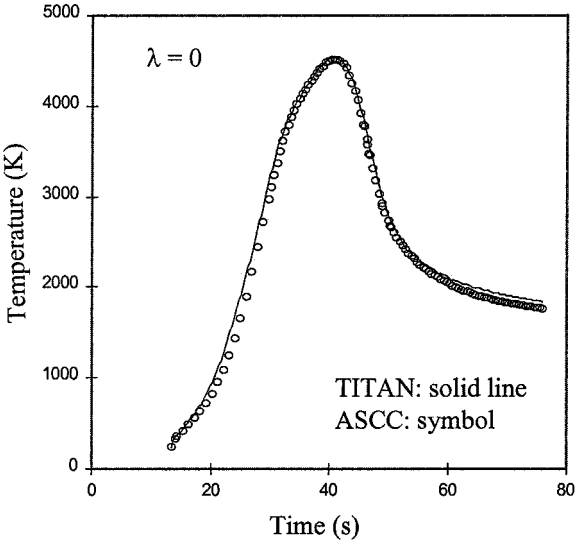

Fig. 8b Stagnation point temperature history predicted for slender body.

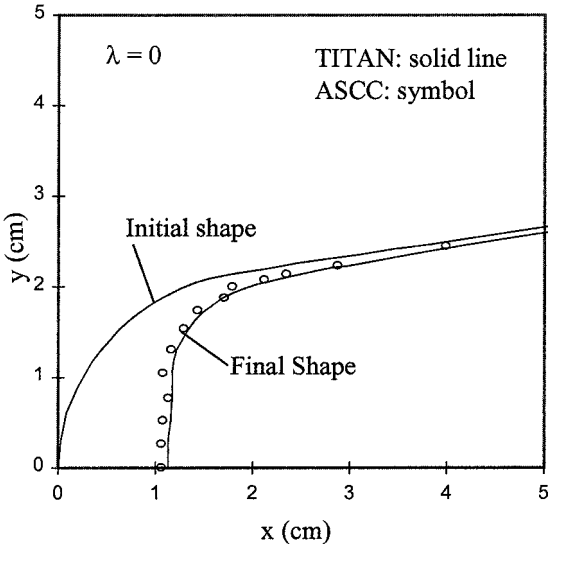

Fig. 8c Shape change predicted for slender body.

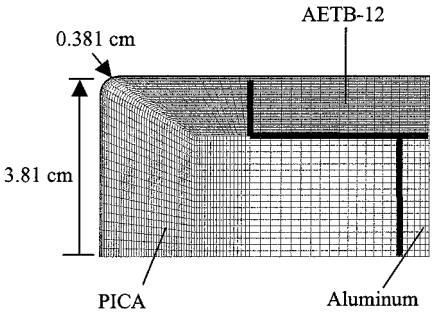

Fig. 9a Computational grid for flat-faced cylindrical arcjet test model.

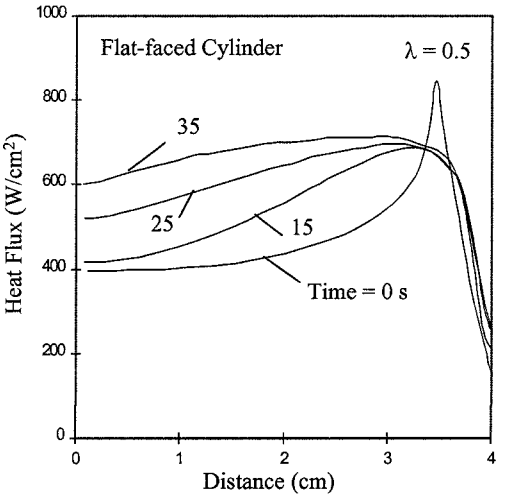

Fig. 9b Surface heating distributions on arcjet model at various times (showing effect of shape change).

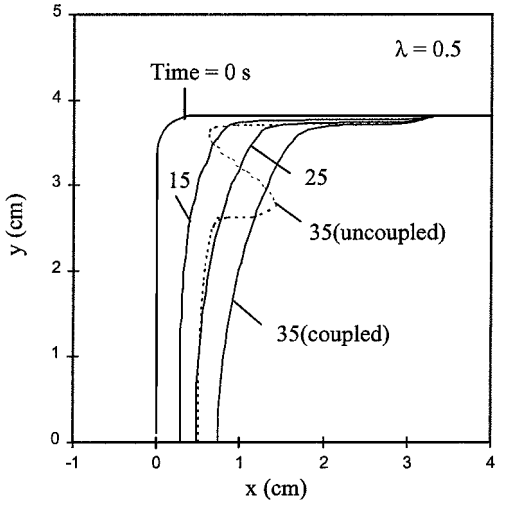

Fig. 9c Surface contours of arcjet model at various times (dotted line shows incorrect uncoupled shape).

result of shape change, the heat flux distribution around the nose region becomes more uniform toward the end of heat pulse.

For both TITAN/GIANTS test cases, an uncoupled calculation was also performed for comparison purposes. In each case the initial heating profile at $t = 0$, from Figs. 9b and 10a, were used for the duration of the heat pulse, and the resulting surface contours are presented as dotted lines in Figs. 9c and 10b, respectively. In each case a nonphysical result is obtained: for the blunt arcjet shape, the shape indents near the corner (Fig. 9c), whereas for the slender body the nosetip becomes indented (Fig. 10b). These examples clearly demonstrate why CFD grids and solutions need to be recalculated for problems with significant shape change.

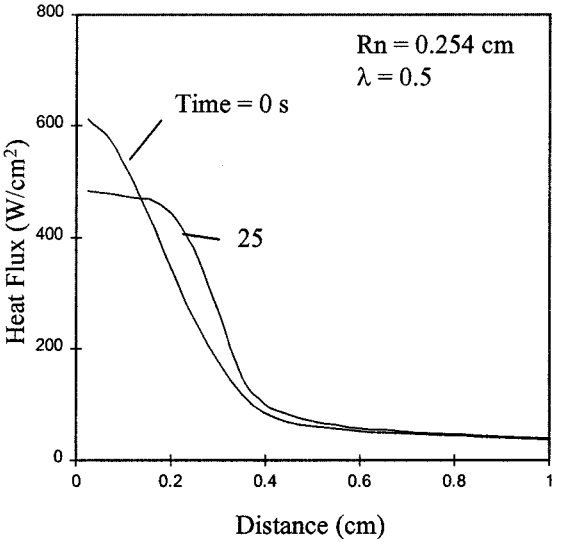

Fig. 10a Surface heating distributions on slender body at 0 and 25 s (showing effect of shape change).

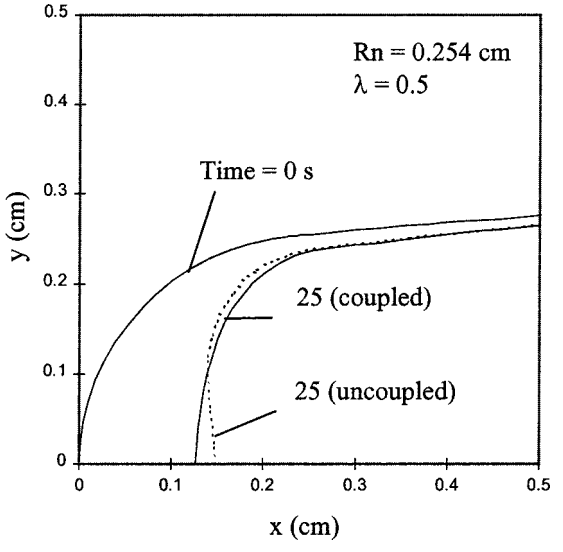

Fig. 10b Surface contours of slender body at 0 and 25 s (dotted line shows incorrect uncoupled shape).

Conclusions

The TITAN program for predicting charring material ablation and shape change has been developed. From benchmark calculations, it has been confirmed that TITAN solutions are consistent with finite element thermal response solutions of MARC, one-dimensional pyrolysis and ablation simulations of FIAT, and axisymmetric shape change calculations of ASCC. High-fidelity, fully coupled, multidimensional solid–fluid simulations for typical arcjet models also were successfully demonstrated using the integrated TITAN/GIANTS procedures. A flat-faced cylinder model and a slender body nosetip were studied. The results indicate that shape change cannot be correctly predicted without using the fully coupled solid–fluid computation because the aeroheating environment and body geometry strongly affect each other. Uncoupling the phenomena can produce unrealistic numerical solutions. TITAN is expected to be useful for the development of thermal response models for ablators using arcjet test data and for the flight simulation of ablating slender body nosetips.

Appendix: Grid Resolution Example

The blunting of the flat-faced arcjet model (Fig. 9) is the most computationally challenging problem presented in this work. This case includes both pyrolysis and recession, and the shape change produces a large change in heat flux profile over time. To provide an example of the grid resolution and accuracy of TITAN, solutions were obtained for the three grids presented in Fig. A1 with grid parameters listed in Table A1. The solutions of Fig. 9 were obtained using grid 2. Grid 1 is coarser, and grid 3 is finer. Each solution used the automatic, adaptive time step and grid movement algorithms; that is, there was no attempt to force the three solutions to use comparable time steps or grid movement.

Figure A2 shows the initial and final surface heat flux distributions. Initially, the three solutions are almost identical, but small differences occur over time as the shape changes. The trend is a prediction of slightly lower heating at the nose with finer grid resolution, but the difference in heat flux is less than 2% at all times for the two finest grids. Figure A3 presents the final shapes calculated using the three grids. After 35 s of heating and about 0.75 cm of recession, the three solutions are very close to each other.

Table A1 Grid parameters

Grid	*jp*	*jl*	*il*
1	21	45	59
2	21	69	59
3	41	89	117

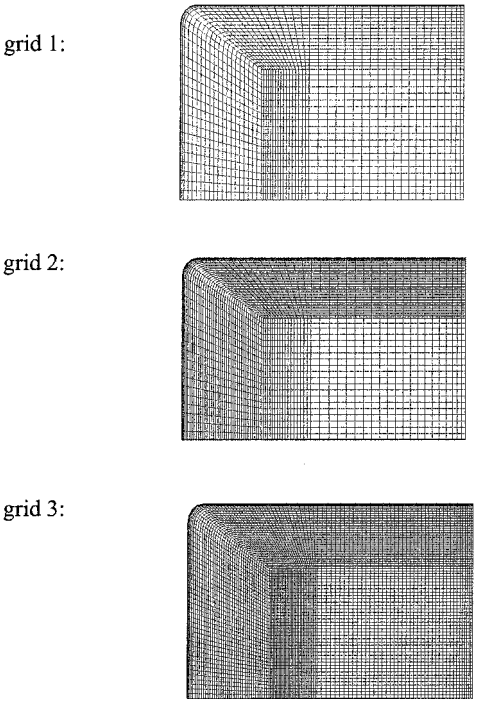

Fig. A1 Three grids for arcjet model.

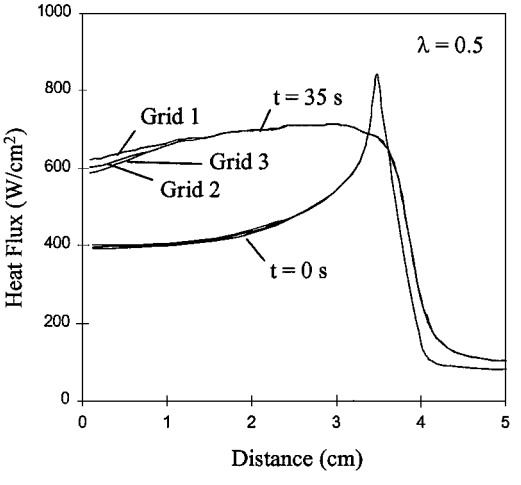

Fig. A2 Initial and final surface heating distributions on arcjet model for three grids.

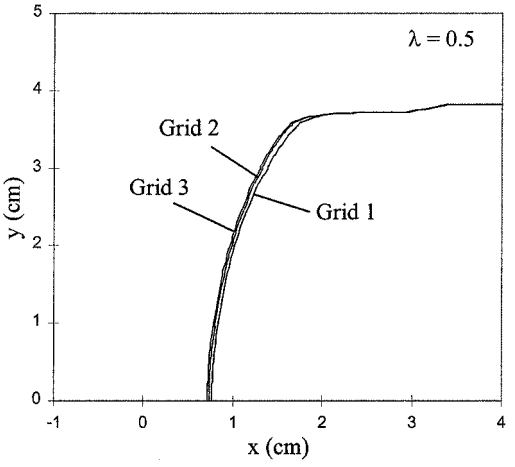

Fig. A3 Final surface contours of arcjet model for three grids.

References

[1]Moyer, C. B., and Rindal, R. A., "Finite Difference Solution for the In-Depth Response of Charring Materials Considering Surface Chemical and Energy Balances," NASA CR-1061, June 1968.

[2]Chen, Y.-K., and Milos, F. S., "Ablation and Thermal Analysis Program for Spacecraft Heatshield Analysis," *Journal of Spacecraft and Rockets*, Vol. 36, No. 3, 1999, pp. 475–483.

[3]King, H. H. C., Muramoto, K. K., Murray, A. L., and Pronchick, S. W., "ABRES Shape Change Code (ASCC 86): Technical Report and User's Manual," Rept. FR-86-24/ATD, Acurex Corp., Mountain View, CA, Dec. 1986.

[4]Chen, Y.-K., Milos, F. S., Bull, J. D., and Squire, T. H., "Integrated Analysis Tool for Ultrahigh-Temperature Ceramic Slender-Body Reentry Vehicles," AIAA Paper 99-0350, Jan. 1999.

[5]Hogan, R. E., Blackwell, B. F., and Cochran, R. J., "Application of Moving Grid Control Volume Finite Element Method to Ablation Problems," *Journal of Thermophysics and Heat Transfer*, Vol. 10, No. 2, 1996, pp. 312–319.

[6]Kuntz, D. W., Hassan, B., and Potter, D. L., "Iterative Approach for Coupling Fluid/Thermal Predictions of Ablating Hypersonic Vehicles," AIAA Paper 99-3460, June 1999.

[7]Candler, G. V., "Computation of Hypersonic Ionized Flows in Chemical and Thermal Nonequilibrium," AIAA Paper 88-0511, Jan. 1988.

[8]Chen, Y.-K., and Henline, W. D., "Analysis of Hypersonic Arcjet Flowfields and Surface Heating of Blunt Bodies," AIAA Paper 93-0272, Jan. 1993.

[9]"User's Manual: Aerotherm Charring Material Thermal Response and Ablation Program CMA87," Rept. UM-87-11/ATD, Acurex Corp., Mountain View, CA, Aug. 1987.

[10]Squire, T. H., Milos, F. S., Hartlieb, G. C., and Rasky, D. J., "TPSX: Thermal Protection Systems Expert and Material Property Database," *ICCE/4, Fourth International Conference on Composites Engineering*, edited by D. Hui, International Community for Composites Engineering and College of Engineering, Univ. of New Orleans, New Orleans, LA, 1997, pp. 937, 938.

[11]"User's Manual: Aerotherm Chemical Equilibrium Computer Program (ACE81)," Rept. UM-81-11/ATD, Acurex, Mountain View, CA, Aug. 1981.

[12]Milos, F. S., and Chen, Y.-K., "Comprehensive Model for Multicomponent Ablation Thermochemistry," AIAA Paper 97-0141, Jan. 1997.

[13]Kays, W. M., and Crawford, M. E., *Convective Heat and Mass Transfer*, 2nd ed., McGraw–Hill, New York, 1980, pp. 355–357.

[14]Kolodziej, P., Bull, J. D., Milos, F. S., and Squire, T. H., "Aerothermal Performance Constraints for Small Radius Leading Edges Operating at Hypervelocity," *Eighth Annual Thermal and Fluids Analysis Workshop on Spacecraft Analysis and Design*, NASA CP-3359, 1997, pp. 9-1–9-7.

[15]*Users Manual, MARC Analysis Research Corporation, Volume A: Users Information*, MARC Analysis Research Corp., Palo Alto, CA, 1994, pp. A1.1–A1.8.

[16]*Users Manual, MARC Analysis Research Corporation, Volume E: Demonstration Problems*, MARC Analysis Research Corp., Palo Alto, CA, 1994, pp. E5.0.1–5.18.8.

[17]Bull, J. D., Rasky, D. J., and Karika, J. C., "Characterization of Selected Diboride Composites," *16th Conference on Metal Matrix, Carbon, and Ceramic Matrix Composites*, edited by J. D. Buckley, NASA CP-3175, Pt. 1, Jan. 1992, pp. 247–265.

[18]Tran, H., Johnson, C., Rasky, D., Hui, F., Chen, Y.-K., and Hsu, M., "Phenolic Impregnated Carbon Ablators (PICA) for Discovery Class Missions," AIAA Paper 96-1911, June 1996.

[19]Tran, H., Johnson, C., Rasky, D., Hui, F., and Hsu, M., "Silicone Impregnated Reusable Ceramic Ablators for Mars Follow-On Missions," AIAA Paper 96-1819, June 1996.

M. Torres
Associate Editor